Physics of Plasmas

Progress on observations of interspecies ion separation in inertial-confinement-fusion implosions via imaging x-ray spectroscopy

Cite as: Phys. Plasmas **26**, 062702 (2019); https://doi.org/10.1063/1.5092998
Submitted: 15 February 2019 . Accepted: 16 May 2019 . Published Online: 04 June 2019

T. R. Joshi, S. C. Hsu, P. Hakel, N. M. Hoffman, H. Sio, and R. C. Mancini

Physics of Plasmas ARTICLE scitation.org/journal/php

Progress on observations of interspecies ion separation in inertial-confinement-fusion implosions via imaging x-ray spectroscopy

Cite as: Phys. Plasmas **26**, 062702 (2019); doi: 10.1063/1.5092998
Submitted: 15 February 2019 · Accepted: 16 May 2019 ·
Published Online: 4 June 2019

T. R. Joshi,[1,a)] S. C. Hsu,[1] P. Hakel,[1] N. M. Hoffman,[1] H. Sio,[2] and R. C. Mancini[3]

AFFILIATIONS

[1]Los Alamos National Laboratory, Los Alamos, New Mexico 87545, USA
[2]Plasma Science and Fusion Center, Massachusetts Institute of Technology, Cambridge, Massachusetts 02139, USA
[3]Physics Department, University of Nevada, Reno, Nevada 89557, USA

[a)]tjoshi@lanl.gov

ABSTRACT

We report on the analyses of x-ray-imaging spectroscopy data from experiments to study interspecies ion separation in direct-drive inertial-confinement-fusion experiments on the Omega laser facility. This is a continuation of recent, related research [S. C. Hsu *et al.*, Euro Phys. Lett. **115**, 65001 (2016); T. R. Joshi *et al.*, Phys. Plasmas **24**, 056305 (2017)]. The targets were argon (Ar)-doped, deuterium (D_2)-filled spherical plastic shells of varying D_2-Ar relative and total gas pressures. We used a time- and space-integrated spectrometer, streaked crystal spectrometer, and up to three time-gated multi-monochromatic x-ray imagers (MMIs) fielded along different lines of sight to record x-ray spectral features obtained from the implosions. The MMI data were recorded between first-shock convergence and slightly before the neutron bang time. We confirm the presence of interspecies ion separation as reported in our recent work. Extensions to the previous work include (a) the inclusion of shell mix in the data analysis, which slightly changes the amount of inferred species separation, (b) observation of species separation closer to the neutron bang time, and (c) fielding of the particle x-ray temporal diagnostic (PXTD) [H. Sio *et al.*, Rev. Sci. Instrum. **87**, 11D701 (2016)] to infer the relative timing between the neutron bang time and peak x-ray emission. Experimentally inferred species separation is compared with radiation-hydrodynamic simulations that include a multi-ion-species transport model.

I. INTRODUCTION

In inertial-confinement-fusion (ICF) experiments, targets are typically spherical plastic or glass shells filled with a fusion-fuel mixture, e.g., DT or D^3He.[1,2] Because of the proven usefulness of elements such as Ar or Kr in x-ray spectroscopy, sometimes small amounts of these elements have also been used in the core along with the main fuel materials for diagnostic purposes.[3–11] Due to the ablation of target surfaces by laser beams or x-rays, the shell implodes and creates several shocks traveling inward across the fuel. The pressure and temperature gradients in the imploding target can drive ion species separation[12,13] via interspecies ion diffusion (e.g., baro-, thermo-, and electro-diffusion).[14–17] Several ICF experimental campaigns[18–26] have reported yield or yield-ratio anomalies where interspecies ion separation within the hot spot is a possible explanation. However, all these campaigns relied on comparing total yield measurements with standard radiation-hydrodynamic simulations that do not model multi-ion-species physics. Recently, standard implosion codes are being upgraded by incorporating the first-principles analytical theories for multi-ion-species diffusion to estimate quantitatively the effect of interspecies ion separation in ICF implosions.[27–29] Similarly, ion-Fokker-Planck[30,31] and particle-in-cell kinetic simulations[18,32,33] are also being used to study ICF implosions in kinetic scenarios.

Our earlier experimental campaign on interspecies ion separation in ICF implosions[34,35] provided direct experimental evidence for interspecies ion separation in an ICF implosion via detailed analysis of imaging x-ray spectroscopy data. In this paper, we provide the results from the analysis of imaging x-ray spectroscopy data from our second interspecies ion separation experimental campaign. Here, we briefly recall the theory that guided our experimental campaign designs (both the previous and present campaigns at OMEGA). The theory predicts that interspecies diffusion is larger for species with larger mass and charge differences.[16] Thus, to increase the chance of observing species separation in our experiments, we focus on implosions with D_2/Ar fill rather than $D/^3He$ or D/T. We chose Ar in particular because of its

proven usefulness as an x-ray spectroscopic tracer in ICF implosions. The theory also predicts that the ion thermo-diffusion ratio maximizes, for a D/Ar plasma, with an Ar atomic concentration of around 1%,[34] thus motivating us to conduct experiments at and near this value. As in our previous publications,[34,35] we interpret observations of any deviation of the Ar ion number fraction from the spatially uniform target pre-fill value as proof of interspecies ion separation in the implosion core. The main objectives of this campaign were to (a) confirm the observation of interspecies ion separation reported in our previous work, (b) investigate the effect of shell-fuel mixing on the experimental inference of interspecies ion separation, (c) compare experimental observations of interspecies ion separation with radiation hydrodynamic simulations that incorporate a multi-ion-species transport model,[16,29,36–38] and (d) explore the dependence of interspecies ion separation on the relative concentration of the heavier species to further validate the theory. Here, we report on each of these objectives in detail. The structure of this paper is as follows. In Sec. II, we provide the details of our OMEGA direct-drive ICF experiments. Section III reports the results from the analysis of multi-monochromatic x-ray imager (MMI)[39] data and particle x-ray temporal diagnostic (PXTD)[40] measurements. Section IV summarizes this paper.

II. EXPERIMENTS AT OMEGA

Direct-drive ICF experiments were performed on the OMEGA laser facility[41] of the Laboratory for Laser Energetics at the University of Rochester, NY, using 60 laser beams. All laser beams were configured to have the same energy and delivered ≈27 kJ of UV laser energy on a target with a 1-ns square pulse shape. The targets were spherical plastic shells (outer radius ≈433–438 μm) of 15 μm thickness with either 15- or 10-atm of D_2 gas fill. For every target with 10-atm of D_2 gas fill, the Ar fraction was either 1.0% or 0.3% of total gas atoms present in the target core. Similarly, for every target with 15-atm of D_2 gas fill, the Ar fraction was either 0.3% or 0.1% of total gas atoms present in the target core. Thus, we had four different types of targets based on the combinations of various pressures of D_2/Ar gas. The core fuel pressures in the targets of this campaign were higher than those in the previous campaign[34,35] with a goal of observing slightly lower-temperature and more-symmetric implosions compared to the previous campaign. Higher fill pressure for otherwise the same target and laser drive increases collisionality and suppresses the interspecies ion separation (see Appendix B). Therefore, we did not increase the D_2 fill pressure in our targets above 15 atm. The Ar K-shell emissions from the core were primarily observed around the time of the first shock convergence to the burning phase of the implosion and recorded using a streaked crystal x-ray spectrometer (mounted on TIM 6, where TIM stands for "10-in. manipulator" diagnostic port), a time- and space-integrated, absolutely calibrated x-ray spectrometer (mounted on TIM 3), and three gated, MMI instruments mounted on three different lines of sight TIM1, TIM 2, and TIM 4. The TIM2 and TIM4 were quasi-orthogonal with each other, but other two combinations TIM1 and TIM4 and TIM1 and TIM2 were not quasi-orthogonal views. Standard neutron diagnostics (12-m neutron time-of-flight scintillator and cryogenic neutron temporal diagnostic) and full-aperture backscatter systems were also fielded. The streaked crystal spectrometer recorded temporally and spectrally resolved but spatially integrated x-ray image data obtained from the implosion core. The MMI instrument recorded spectrally, spatially, and temporally resolved implosion core images.[4] The spatial resolution of MMI instrument is ≈10 μm. The spectral resolving power of the MMI is $E/\Delta E \approx 150$,[4] i.e., for Ar with the spectral range of 3000 to 5500 eV, it is ≈20 eV. Each MMI recorded four snapshots of the implosion with a temporal resolution of ≈100 ps. The time of each frame of MMI data is approximately known based on the experimental trigger time of each frame of the x-ray framing camera, but due to cable delays and the finite time of the sweep across the cameras photocathode strips, we regard the quoted times as having an uncertainty ≈50 ps. The MMI recorded spectrally resolved implosion core images on four MCPs, i.e., four frames (Frame-1 is the earliest, and Frame-4 is the latest in time) in the spectral range of 3.3–5.5 keV around the time of the first shock convergence and burning phase. We were able to record good quality x-ray image data, including line and continuum emission, from all of the target types with the MMI fielded along three lines of sight, SSCA and XRS instruments. The yield (DD-n) and burn-weighted ion temperature were obtained from the 12-m neutron time-of-flight scintillator. Similarly, the neutron bang time and the burn width were obtained from the cryogenic neutron temporal diagnostic (cryo-NTD). In this paper, the experimental trigger times of different frames of the MMI instrument and neutron bang time in implosions are given relative to the leading edge of the laser pulse. The details about the MMI instrument, the data processing method, and the extractions of narrowband images and space-resolved spectra are described elsewhere.[4,5,42] For this work, we reconstructed narrowband images of Ar Heβ and Lyβ from the MMI data. Similarly, space-resolved spectra were extracted from the annular regions on the core images across the MMI data.[35] Figure 1(a) shows the MMI data from shot 86684 TIM 2 which consists of data recorded by four strips, and Fig. 1(b) shows the Ar Heβ and Lyβ narrow-band images constructed from 80 eV wide spectral ranges across the photon energies of the respective lines from the Frame-4, i.e., bottom frame. We used 3640–3720 eV and 3895–3975 eV bands to reconstruct Heβ and Lyβ, respectively. The photon energy values for Heβ and Lyβ are 3680 eV and 3935 eV, respectively. Because x-ray emission is so central to the MMI measurement, on this campaign, we also fielded the PXTD[40] (on TIM5) in order to obtain information on the relative timing between the neutron bang time and the x-ray emission peak.

III. DATA ANALYSIS AND RESULTS

The analysis methods to infer spatial profiles of plasma conditions, D and Ar ion number densities, and Ar ion number fractions in the implosion core remain the same as in the analyses of previous campaign's data. The details of the analysis methods, Ar atomic kinetics modeling, and calculation of the x-ray spectral emission were described in our previous publication.[35] The method of error analysis in the MMI data is also the same as that described in our previous publication.[35] Briefly, the analysis methods to infer the Ar atom number fraction spatial profile consist of three steps. The first step is to extract electron temperature (T_e) and density (n_e) spatial distributions in the implosion core by using an emissivity analysis method. In the

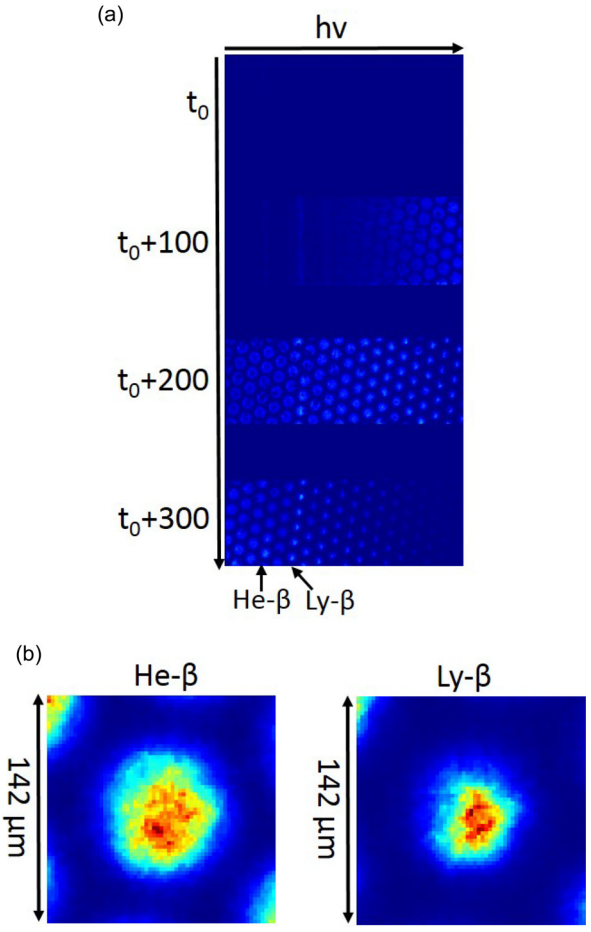

FIG. 1. (a) Sample MMI data from shot 86684 TIM 2. It consists of data recorded by four strips (i.e., frames) (b) Ar Heβ and Lyβ narrow-band images constructed from 80-eV wide spectral ranges across the photon energies of the respective lines from Frame-4, i.e., bottom frame.

second step of the analysis, we extract spatial distributions of the Ar ion number density (n_{Ar}) by using an inversion method based on the proportionality between the intensity of a line emission and the corresponding excited-level population density. Spectral intensities in MMI data are in arbitrary units. n_{Ar} in absolute units is obtained by assuming conservation of Ar atoms in the implosion core. The final step uses the charge quasi-neutrality constraint to obtain the deuterium ion number density (n_D) and the Ar ion number fraction (f_{Ar}). Ar Heβ and Lyβ narrow-band images constructed from 80-eV wide spectral ranges across the photon energies of the respective lines have been used in the analyses. These lines are considered optically thin.[7,11] In this work, we have updated the charge quasi-neutrality step of the analysis method to include the mixing of shell materials into the implosion core. An example of data analysis results from this experimental campaign is shown in Figs. 2(a) and 2(b).

Figure 2(a) shows the spatial profiles of electron temperature and density in the implosion core obtained from the analyses of the MMI data from the shot 86684 TIM2 Frame-4. The frame trigger time and the neutron bang time (BT) were 1.390 ns and 1.466 ns relative to the leading edge of the laser pulse, respectively. Similarly, the spatial profiles of Ar and D ion number densities in the implosion core for the same data are shown in Fig. 2(b).

A. Observation of the Ar ion fraction vs core radius in different types of targets

In this OMEGA campaign, we had total of four different types of targets with three different Ar concentrations and two different D_2 fill pressures. Detailed analyses of the MMI data provided the Ar ion number fraction vs core radius from all of the target types; all of them deviated from their pre-fill values. As stated in our previous publications,[34,35] deviation of the Ar ion number fraction from the spatially uniform target pre-fill value constitutes proof of interspecies ion separation in the implosion core. Hence, we have obtained experimental evidence of interspecies ion separation in the implosion cores of all of the target types from this campaign. This observation reconfirms our earlier experimental evidence of interspecies ion separation in an ICF implosion core via imaging x-ray spectroscopy.[34,35] Table I provides the summary of the shots included in the MMI data analysis for this paper.

Figures 3(a) and 3(b) show plots for the Ar ion number fraction (% by total atoms) vs core radius from the analysis of MMI data obtained from the targets with 10 and 15 atm of D_2 fill, respectively. In Fig. 3(a), the red and blue plots are obtained from the analyses of MMI data from shot 86677 TIM 1 Frame-3 (Ar pre-fill: 1.0%) and shot 86684 TIM 2 Frame-4 (Ar pre-fill: 0.3%), respectively. The MMI

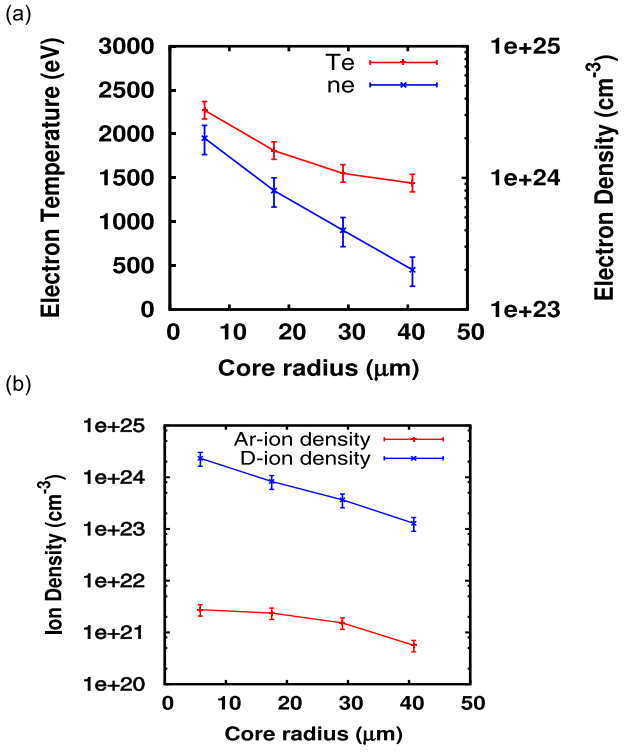

FIG. 2. (a) Spatial profiles of electron temperature and density. (b) Spatial profiles of Ar and D ion number densities in the implosion core from the analyses of the shot 86684 TIM 2 Frame-4 MMI data.

TABLE I. Summary of the shots included in the MMI data analysis for this paper. Yield (DD-n) and burn-weighted ion temperature $\langle T_i \rangle$ are from the 12-m neutron time-of-flight scintillator, and neutron bang times (BT) and burn widths (BW) are from the cryogenic neutron temporal diagnostic (cryoNTD). Note that BT corresponds to compression burn in these implosions.

Shot #	Laser energy (kJ)	Capsule OD (μm)/ CH thickness (μm)	D_2 fill (atm)	Ar (atom%)	Yield (DD-n)	$\langle T_i \rangle$ (keV)	BT (ns)	BW (ps)
86677	27.3	874/15	10.0	1.0	1.80E11	5.86	1.465	140
86678	27.5	869/15	15.0	0.3	2.89E11	5.53	1.475	147
86680	27.4	872/15	15.0	0.1	3.28E11	5.24	1.461	152
86684	27.5	874/15	10.0	0.3	2.77E11	6.14	1.466	132

data recording time for shot 86677 TIM 1 Frame-3 was 1.250 ns, and the neutron bang time for this shot was 1.465 ns. Thus, the MMI data for this case were recorded at ≈85% of the neutron bang time in the implosion. Similarly, the MMI data recording time for shot 86684 TIM 2 Frame-4 was 1.390 ns, and the neutron bang time for this shot was 1.466 ns. Hence, the MMI data record time for this case becomes ≈95% of the neutron bang time. The red and blue plots in Fig. 3(b) are obtained from the analyses of MMI data from shot 86678 TIM 1 Frame-3 (Ar pre-fill: 0.3%) and shot 86680 TIM 2 Frame-4 (Ar pre-fill: 0.1%), respectively. The MMI data recording time for shot 86678 TIM2 Frame-4 was 1.380 ns, and the neutron bang time for this shot was 1.475 ns. The MMI data were recorded at ≈94% of the neutron bang time. Similarly, The MMI data record time for shot 86680 TIM 1 Frame-3 was 1.40 ns, and the neutron bang time for this shot was 1.461 ns. In this case, the MMI data record time becomes ≈96% of the neutron bang time. Thus, this experimental campaign provides an experimental evidence of interspecies ion separation till 96% of the neutron bang time. The previous campaign provided such an evidence up to 87% of the neutron bang time. This campaign has provided an experimental evidence of the interspecies ion separation persisting in an ICF implosion core much closer to the neutron bang time.

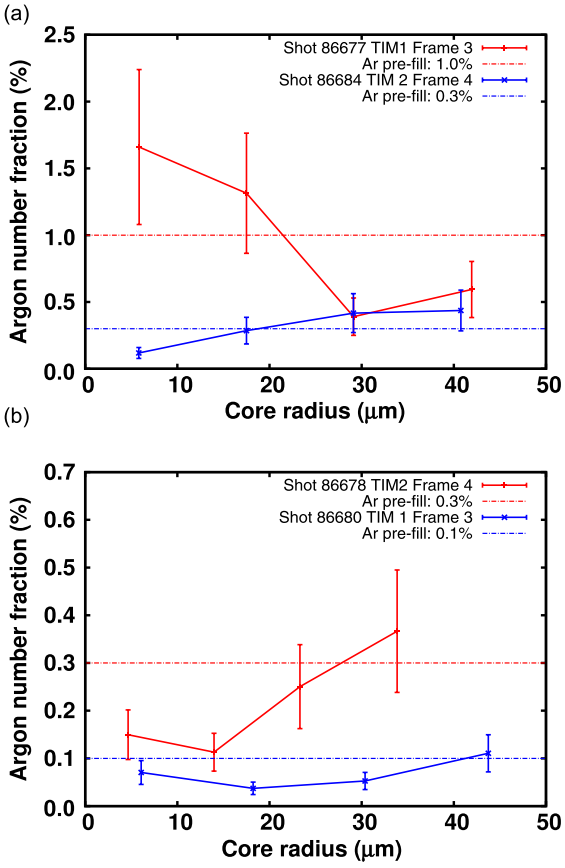

FIG. 3. (a) Ar ion number fraction vs implosion core radius from the analysis of MMI data obtained from the targets with 10 atm of D_2-fill. The red plot is from shot 86677 TIM 1 Frame-3 (Ar pre-fill: 1.0%, trigger time = 1.250 ≈ 85% of neutron BT) and the blue plot is from shot 86684 TIM 2 Frame-4 (Ar pre-fill: 0.3%, trigger time = 1.390 ≈ 95% of neutron BT). (b) Ar ion number fraction vs implosion core radius from analysis of MMI data obtained from the targets with 15 atm of D_2 fill. The red plot is from shot 86678 TIM 1 Frame-3 (Ar pre-fill: 0.3%, trigger time = 1.380 ≈ 94% of neutron BT) and shot 86680 TIM 2 Frame-4 (Ar pre-fill: 0.1%, trigger time = 1.40 ≈ 96% of neutron BT).

One of the important objectives of this experimental campaign was to investigate the dependency of interspecies ion separation on various concentrations of the heavier ion species present in the core. Figures 4(a) and 4(b) show the percentage deviation of Ar ion number fractions from their respective pre-fill values for the profiles shown in Figs. 3(a) and 3(b). The MMI data to infer the profiles in Fig. 4(b) were recorded at ≈95% of the neutron bang time in the implosions. The red (86677 TIM1 Frame-3) curve in Fig. 4(a) was recorded at ≈85% of the bang time, while blue was recorded at ≈95% of the bang time in the implosions. Unfortunately, we do not have any good quality analyzable MMI data available from this type of target recorded approximately at the same time as of the blue curve shown in Fig. 4(a) and vice versa. The red plot is the closest available MMI data for blue in Fig. 4(a) in terms of the MMI data recording time in the implosions. We did not observe weaker or stronger interspecies ion separation depending on the various concentrations of heavier ion species in the core. This could be due to the reason that we changed the Ar concentrations only by ≈3 times in the targets of the same D_2 fill pressure. There could be little differences in the observed interspecies ion separation depending on the concentration of Ar ions in the core, but the uncertainties associated with the MMI data and the analysis method make it indistinguishable.

B. Comparison of MMI data analysis results with simulations

In our previous work,[34,35] we reported the comparison of the experimental observations of interspecies ion separation from our

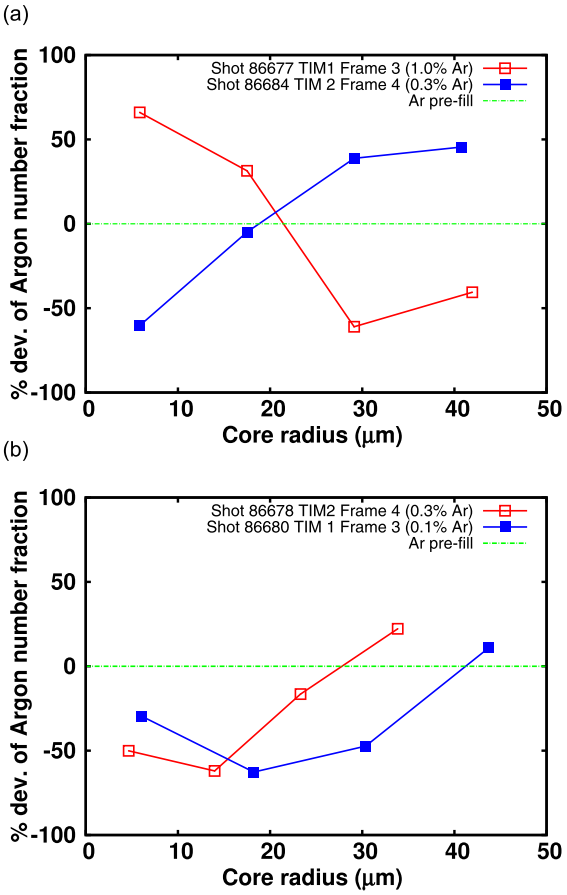

FIG. 4. Percentage deviation of the Ar ion number fraction from their respective pre-fill value (a) for the profiles shown in Fig. 3(a) and (b) for the profiles shown in Fig. 3(b).

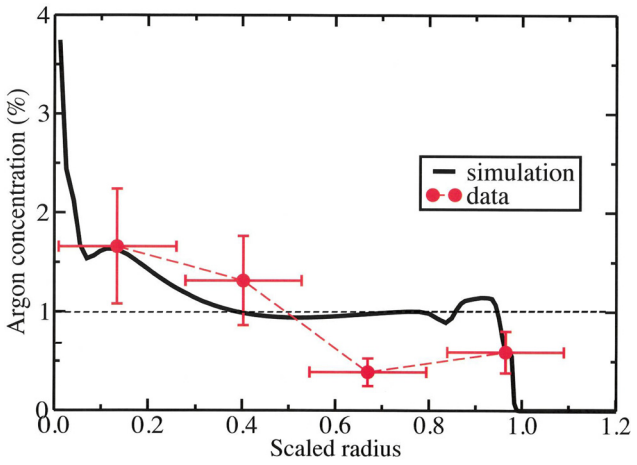

FIG. 5. Comparison of profiles of the Ar number fraction vs implosion core radius obtained from 1D post-shot ZPKZ simulation and MMI data analysis for shot 86677 TIM 1 Frame-3.

previous campaign with the simulations obtained from the xRAGE[27,28,43] with a two-ion-species transport model. In this work, we performed post-shot 1D radiation hydrodynamic simulations with a multi-ion-species transport model (ZPKZ)[16,29,36–38] to support our observation of experimental evidence of interspecies ion separation from the analysis of the MMI data obtained from our second interspecies ion separation experimental campaign on the Omega laser facility. As an example, Fig. 5 shows the comparison of profiles of the Ar number fraction vs core radius obtained from 1D post-shot ZPKZ simulation and MMI data analysis for shot 86677 TIM 1 Frame-3. The MMI data recording time and the neutron bang time were 1.25 ns and 1.465 ns, respectively. Thus, the MMI data were recorded ≈ at the 85% of the neutron bang-time. While detailed validation is beyond the scope of this work, we have found reasonable agreement between data and simulation for shot 86677 TIM 1 Frame-4.

In Fig. 5, our interpretation is that the shock has rebounded from the center, and the effect of the rebounding shock on species separation is argon depletion (equivalently, D enhancement) in front of the shock and argon enhancement behind the shock. The shell-gas interface, defined as the location of equal concentration of hydrogen, carbon, and deuterium, is assigned the scaled radius of 1 in this plot. We have overlapped the radius of the experimental implosion core (maximum value in the red curve) with the maximum radial value in the simulated (scaled) curve (≈1) in the figure for the comparison purpose. Specifically, the red curve (experimental) shows a higher argon concentration for $r \leq 0.5$ and a lower Ar concentration for $r \geq 0.5$, which indicates the location of the rebounding shock around 0.5 (≈23 μm in the experimental implosion core) propagating outward. In the black curve (simulated), we also see a decrease in the Ar concentration for $r \geq 0.5$ compared to $r \leq 0.5$. The vertical error bars in the experimental data are obtained from the uncertainties in the experimental data and the systematic errors in the analysis method.[35] The horizontal bars in the experimental profile represent the extent of the spatial zone represented by each data point.

C. Effect of mixing of shell materials into the hot core

In our previous work, we had not included shell-fuel mixing in our analysis method to investigate its effect on the interspecies ion separation. There, we showed the comparisons of experimental observation of interspecies ion separation and xRAGE simulations with a two-ion-species transport model. The experimental determination of the Ar ion number fraction vs core radius was subject to the neglect of CH mixing into the hot spot. Here, we have assessed the differences in the experimentally inferred interspecies ion separation with or without including shell-fuel mixing in our analysis method. If plastic from the shell, consisting of carbon (C) and hydrogen (H), mixes into the fuel, then the core electron density has now four contributions from the ionization of Ar, D, C, and H atoms. Thus, we use the following charge-quasi neutrality constraint to extract deuterium ion number density:

$$n_e = n_{Ar} Z_{Ar}(T_e, n_e) + n_D Z_D(T_e, n_e) + n_C Z_C(T_e, n_e) + n_H Z_H(T_e, n_e). \quad (1)$$

In Eq. (1), the ionization balances for Ar, D, C, and H at the given T_e and n_e (experimentally inferred spatial profiles) are computed by

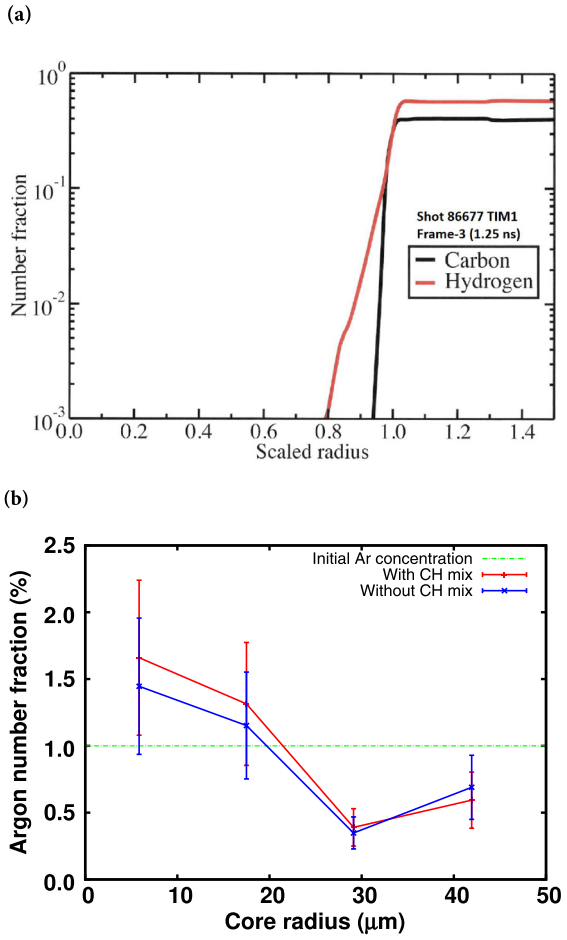

FIG. 6. (a) Simulations of plastic (carbon and hydrogen) mixing into the implosion core. These profiles were computed by using ZPKZ simulations. (b) Ar number fraction vs core radius with and without including plastic mixing into the implosion core for shot 86677 TIM 1 Frame-3.

using the LANL suite of atomic codes.[44–47] The argon ion density, i.e., n_{Ar}, is extracted experimentally before this step of the analysis.[35] CH mixing profiles were computed via radiation hydrodynamic simulations with a multi-ion species transport model (ZPKZ). The details of the extraction of the spatial profiles of C and H are explained in the Appendix. The only unknown is deuterium ion density. Finally, the Ar ion number fraction (f_{Ar}) is inferred from the following expression as used in our previous work

$$f_{Ar} = \frac{n_{Ar}}{n_{Ar} + n_D}. \quad (2)$$

Figure 6(a) shows the simulations of carbon and hydrogen ion number fractions mixed into the implosion core. These profiles were computed using ZPKZ simulations. Figure 6(b) shows the Ar number fraction vs implosion core radius with and without including plastic mixing into the implosion core for shot 86677 TIM 1 Frame-3. The inclusion of the shell material in the charge quasi-neutrality step of the analysis slightly changes Ar enhancement and depletion.

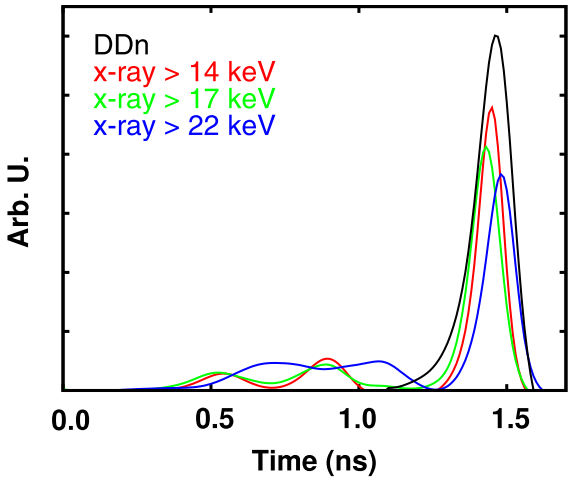

FIG. 7. Time history of DDn and x-rays (measured by 3 channels of the PXTD) for shot 86671.

D. Relative timing between the neutron bang time and the x-ray peak

The PXTD[40] provides spatially integrated time histories of both the neutron production rate and x-ray emission (3 channels with energies >14, >17, and >22 keV, respectively) on the same time axis, with relative timing uncertainties of 10–20 ps. While the PXTD data are at higher energies than those for the Ar K-shell emission recorded by the MMI instruments, Fig. 7 shows that the lower-energy x-rays recorded by the PXTD (>14 keV red curve and >17 keV green curve) occur slightly earlier than the peak of neutron production, and thus, it is inferred that the x-ray peak recorded by the MMI instruments is also earlier than the neutron bang time. Shot 86671 used the same target type as shot 86677, which is featured in the MMI analysis. Table II summarizes all the recorded PXTD data for each case, i.e., for each unique combination of target fill pressure, Ar concentration, and PXTD filter energy. When there were multiple shots per case, we show the average for that case for a given channel. Case 4 has data points for multiple x-ray channels.

IV. CONCLUSIONS

In this paper, we have reported the data analysis results obtained from LANL's second interspecies ion separation experimental campaign via imaging x-ray spectroscopy. We performed a series of direct-

TABLE II. Summary of the recorded PXTD data for each case.

Case #	D_2 fill (atm)	Ar (atom%)	(x-ray BT minus nuclear BT) (ps) channel >22 (keV)	Channel >17 (keV)	Channel >14 (keV)
1	15	0.3	99		
2	10	0.3	88		
3	15	0.1	71		
4	10	1.0	36	−34	−20

drive ICF experiments on the Omega laser facility. The targets were Ar-doped, D_2-filled spherical plastic shells of varying D_2-Ar relative and total gas pressures. We used a time- and space-integrated spectrometer, streaked crystal spectrometer, and up to three gated multi-monochromatic x-ray imagers (MMIs) fielded along different lines of sight to record x-ray spectral features obtained from the implosions. The fuel pressures in the target cores were higher than our last campaign with a goal of observing lower temperature, more symmetric implosions. The timing of the recording of the MMI data in the implosion was in between first-shock convergence and slightly before the neutron bang time.

Detailed analyses of the MMI data from this campaign confirmed the presence of interspecies ion separation in direct-drive ICF implosion core reported in our previous work. The inclusion of shell materials into the implosion cores in the analysis method slightly changed the Ar enhancement and depletion in the core compared to the exclusion of the mixing of shell materials into the core. We observed improved symmetry in the implosions of the current campaign compared to the implosions in the previous campaign, which was an important step to assess our analysis methodology. We observed the persistence of the interspecies ion separation up to 96% of the neutron bang time which is 9% closer to the neutron bang-time compared to the observation in earlier campaign. Within measurement uncertainties, we did not observe relatively weak or strong interspecies ion separation depending on the various concentrations of heavier ion species in the core. In our previous work, we compared experimental observation of interspecies ion separation with xRAGE simulations including a two-ion-species transport model. To compare the experimental observation of interspecies ion separation from this campaign, we used radiation-hydrodynamic simulations with a multi-ion-species transport model, the results of which agree well with our observations. The PXTD revealed the relative timing between the neutron bang time and peak x-ray emission. We have confirmed and extended our earlier observations of interspecies ion separation in ICF implosions,[34,35] and we believe that these observations will be useful for further benchmarking and validation of first-principles modeling of multi-ion-species effects in ICF.

ACKNOWLEDGMENTS

We acknowledge R. Aragonez, T. Archuleta, J. Fooks, V. Glebov, M. Schoff, T. Sedillo, C. Sorce, R. Staerker, N. Whiting, B. Yaakobi, R. Shah, and the OMEGA operations team for their support in experimental planning, execution, and providing processed x-ray and neutron data. We acknowledge R. Petrasso of MIT for his encouragement and support for fielding the PXTD on these experiments. This work was supported by the LANL ICF and ASC (Advanced Simulation and Computing) Programs under US-DoE Contract No. DE-AC52-06NA25396.

APPENDIX A: MIXING OF SHELL MATERIALS (PLASTIC) INTO THE IMPLOSION CORE

Figure 6(a) shows the calculated spatial profiles of ion fractions of carbon and hydrogen in the implosion core. The horizontal axis represents the scaled value of the implosion core radius, and the vertical axis represents carbon and hydrogen ion fractions. The scaled radial value of one represents the interface at which three ion species, i.e., deuterium, carbon, and hydrogen, meet with each other. Each ion species fraction is one third of its total value at the scaled radial value 1.

Suppose x_1 and x_2 represent fractions of carbon (C) and hydrogen (H) ions, respectively. We express x_1 and x_2 as follows:

$$x_1 = \frac{n_H}{(n_H + n_D + n_C)}, \tag{A1a}$$

$$x_2 = \frac{n_C}{(n_H + n_D + n_C)}, \tag{A1b}$$

where n_H, n_D and n_C are the ion densities of hydrogen, deuterium, and carbon, respectively. From Eqs. (A1a) and (A1b),

$$n_H = (n_H + n_D + n_C)x_1, \tag{A2a}$$

$$n_C = (n_H + n_D + n_C)x_2. \tag{A2b}$$

Dividing Eq. (A2a) by (A2b), we get,

$$n_C = \frac{x_2}{x_1} n_H. \tag{A3}$$

The charge quasi-neutrality condition for our implosion core can be written as

$$n_e = n_{Ar}Z_{Ar} + n_D Z_D + n_C Z_C + n_H Z_H, \tag{A4}$$

where Z_{Ar}, Z_C, Z_H, and Z_D are the ionization degrees of argon, carbon, hydrogen, and deuterium, respectively. n_{Ar} and n_e are the argon ion and electron densities, respectively. Using average $Z_{Ar} \approx 16$, $Z_C \approx 6$, $Z_H \approx 1$, and $Z_D \approx 1$ in Eq. (A4),

$$n_e \simeq 16n_{Ar} + n_D + 6\frac{x_2}{x_1} n_H + n_H. \tag{A5}$$

Suppose $\alpha = n_{Ar}/n_D$, which can be written as

$$n_{Ar} = \alpha n_D. \tag{A6}$$

Suppose $\gamma = n_H/n_D$, which can be written as

$$n_H = \gamma n_D. \tag{A7}$$

From Eqs. (A3) and (A7), we get,

$$n_C = \gamma \frac{x_2}{x_1} n_D. \tag{A8}$$

Substituting values of n_{Ar}, n_H, and n_C from Eqs. (A6)–(A8) in Eq. (A5), we get,

$$n_e \simeq \left(1 + 16\alpha + 6\frac{x_2}{x_1}\gamma + \gamma\right) n_D. \tag{A9}$$

We obtain values of x_1 and x_2 from the plots in Fig. 6(a) via ZPKZ simulation. From Eqs. (A1a), (A7), and (A8), we get the following relation among γ, x_1 and x_2:

$$\gamma = \frac{x_1}{(1 - x_1 - x_2)}. \tag{A10}$$

Extraction of deuterium ion number density from the charge quasi-neutrality condition can be written as (from Eqs. (A4), (A7), and (A8))

$$n_D = \frac{n_e - n_{Ar} Z_{Ar}}{Z_D + \gamma \frac{x_2}{x_1} Z_C + \gamma Z_H}. \quad \text{(A11)}$$

In our previous work, we used the following emissivity equation (Ar K shell emissions) for the extraction of the spatial profile of electron number density in the implosion core. The emissivity equation[7] without including mixing of shell (shell) materials into the implosion core can be written as follows:

$$\varepsilon_{Line}^{Expm} = k \varepsilon_{Line}^{Theory}(T_e, n_e), \quad \text{(A12)}$$

where k is a scale factor between experimental and theoretical emissivities. The emissivity equation after including the mixing of shell materials (carbon and hydrogen) into the implosion core can be written as

$$\varepsilon_{Line}^{Expm} \simeq \frac{k}{\left(1 + 16\alpha + 6\frac{x_2}{x_1}\gamma + \gamma\right)} \varepsilon_{Line}^{Theory}(T_e, n_e). \quad \text{(A13)}$$

We used Eq. (A13) for the extraction of the spatial profile of electron number density in the implosion cores of our second experimental campaign.

APPENDIX B: INTERSPECIES ION SEPARATION IN IMPLOSIONS WITH HIGHER FUEL DENSITY

Here, we present analysis of MMI data from an earlier Omega implosion,[48] performed by the University of Nevada, Reno, with higher fill pressure (20 atm) compared to the implosions analyzed in Sec. III. Figure 8 shows the Ar number fraction (%) vs implosion core radius for shot 47477 (TIM3, Frame-1, ≈ 200 ps before neutron bang time, 20-atm D_2 fill pressure, 0.17% Ar atom fraction). We used the Ar Heβ (3640–3720 eV) emission to infer the result shown in Fig. 8. The flatter profile compared to results in Sec. III suggests much smaller relative species separation, consistent with the higher collisionality in these higher-fill-pressure targets. Uncertainties are estimated using the same methodology described in our previous publication.[35]

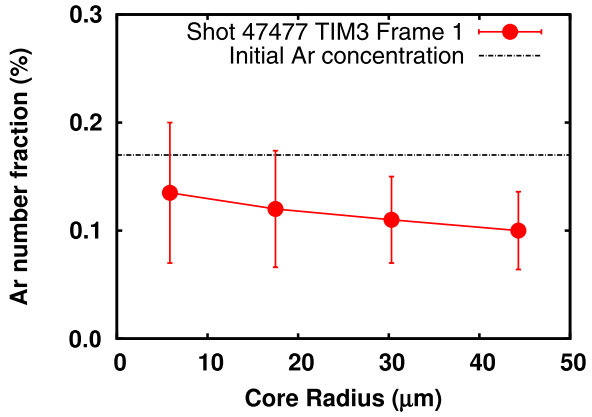

FIG. 8. Ar ion number fraction vs core radius from analysis of MMI data from the University of Nevada, Reno shot 47477 (20-atm D_2 fill pressure, 0.17% Ar atom fraction, ≈ 200 ps before neutron bang time).

REFERENCES

[1] J. D. Lindl, P. Amendt, R. L. Berger, S. G. Glendinning, S. H. Glenzer, S. W. Haan, R. L. Kauffman, O. L. Landen, and L. J. Suter, Phys. Plasmas **11**, 339 (2004).
[2] S. Atzeni, Plasma Phys. Controlled Fusion **51**, 124029 (2009).
[3] I. Golovkin, R. Mancini, S. Louis, Y. Ochi, K. Fujita, H. Nishimura, H. Shirga, N. Miyanaga, H. Azechi, R. Butzbach, I. Uschmann, E. Förster, J. Delettrez, J. Koch, R. W. Lee, and L. Klein, Phys. Rev. Lett. **88**, 045002 (2002).
[4] T. Nagayama, R. C. Mancini, R. Florido, R. Tommasini, J. A. Koch, J. A. Delettrez, S. P. Regan, and V. A. Smalyuk, J. Appl. Phys. **109**, 093303 (2011).
[5] T. Nagayama, R. C. Mancini, R. Florido, D. Mayes, R. Tommasini, J. A. Koch, J. A. Delettrez, S. P. Regan, and V. A. Smalyuk, Phys. Plasmas **21**, 050702 (2014).
[6] S. P. Regan, J. A. Delettrez, R. Epstein, P. A. Jaanimagi, B. Yaakobi, V. A. Smalyuk, F. J. Marshall, D. D. Meyerhofer, W. Seka, D. A. Haynes, I. E. Golovkin, and C. F. Hooper, Phys. Plasmas **9**, 1357 (2002).
[7] L. Welser-Sherrill, R. C. Mancini, J. A. Koch, N. Izumi, R. Tommasini, S. W. Haan, D. A. Haynes, I. E. Golovkin, J. J. MacFarlane, J. A. Delettrez, F. J. Marshall, S. P. Regan, V. A. Smalyuk, and G. Kyrala, Phys. Rev. E **76**, 056403 (2007).
[8] R. Florido, R. C. Mancini, T. Nagayama, R. Tommasini, J. A. Delettrez, S. P. Regan, and B. Yaakobi, Phys. Rev. E **83**, 066408 (2011).
[9] D. A. Haynes, D. T. Garber, C. F. Hooper, R. C. Mancini, Y. T. Lee, D. K. Bradley, J. Delettrez, R. Epstein, and P. A. Jaanimagi, Phys. Rev. E **53**, 1042 (1996).
[10] B. Yaakobi, F. J. Marshall, and R. Epstein, Phys. Rev. E **54**, 5848 (1996).
[11] T. Nagayama, R. C. Mancini, R. Florido, D. Mayes, R. Tommasini, J. A. Koch, J. A. Delettrez, S. P. Regan, and V. A. Smalyuk, Phys. Plasmas **19**, 082705 (2012).
[12] P. Amendt, O. L. Landen, H. F. Robey, C. K. Li, and R. D. Petrasso, Phys. Rev. Lett. **105**, 115005 (2010).
[13] P. Amendt, S. C. Wilks, C. Bellei, C. K. Li, and R. D. Petrasso, Phys. Plasmas **18**, 056308 (2011).
[14] G. Kagan and X. Z. Tang, Phys. Rev. Lett. **109**, 269501 (2012).
[15] G. Kagan and X.-Z. Tang, Phys. Plasmas **19**, 082709 (2012).
[16] G. Kagan and X.-Z. Tang, Phys. Lett. A **378**, 1531 (2014).
[17] G. Kagan, S. D. Baalrud, and J. Daligault, Physics of Plasmas **24**, 072705 (2017).
[18] C. Bellei, P. A. Amendt, S. C. Wilks, M. G. Haines, D. T. Casey, C. K. Li, R. Petrasso, and D. R. Welch, Phys. Plasmas **20**, 012701 (2013).
[19] J. R. Rygg, J. A. Frenje, C. K. Li, F. H. Séguin, R. D. Petrasso, J. A. Delettrez, V. Y. Glebov, V. N. Goncharov, D. D. Meyerhofer, S. P. Regan, T. C. Sangster, and C. Stoeckl, Phys. Plasmas **13**, 052702 (2006).
[20] D. C. Wilson, G. A. Kyrala, J. F. Benage, F. J. Wysocki, M. A. Gunderson, W. J. Garbett, V. Yu. Glebov, J. Frenje, B. Yaakobi, H. W. Herrmann, J. H. Cooley, L. Welser-Sherrill, C. J. Horsfield, and S. A. Roberts, J. Phys. Conf. Ser. **112**, 022015 (2008).
[21] E. S. Dodd, J. F. Benage, G. A. Kyrala, D. C. Wilson, F. J. Wysocki, W. Seka, V. Y. Glebov, C. Stoeckl, and J. A. Frenje, Phys. Plasmas **19**, 042703 (2012).
[22] D. T. Casey, J. A. Frenje, M. Gatu Johnson, M. J.-E. Manuel, H. G. Rinderknecht, N. Sinenian, F. H. Séguin, C. K. Li, R. D. Petrasso, P. B. Radha, J. A. Delettrez, V. Y. Glebov, D. D. Meyerhofer, T. C. Sangster, D. P. McNabb, P. A. Amendt, R. N. Boyd, J. R. Rygg, H. W. Herrmann, Y. H. Kim, and A. D. Bacher, Phys. Rev. Lett. **108**, 075002 (2012).
[23] H. W. Herrmann, J. R. Langenbrunner, J. M. Mack, J. H. Cooley, D. C. Wilson, S. C. Evans, T. J. Sedillo, G. A. Kyrala, S. E. Caldwell, C. S. Young, A. Nobile, J. Wermer, S. Paglieri, A. M. McEvoy, Y. Kim, S. H. Batha, C. J. Horsfield, D. Drew, W. Garbett, M. Rubery, V. Y. Glebov, S. Roberts, and J. A. Frenje, Phys. Plasmas **16**, 056312 (2009).
[24] M. J. Rosenberg, F. H. Séguin, P. A. Amendt, S. Atzeni, H. G. Rinderknecht, N. M. Hoffman, A. B. Zylstra, C. K. Li, H. Sio, M. Gatu Johnson, J. A. Frenje, R.

D. Petrasso, V. Y. Glebov, C. Stoeckl, W. Seka, F. J. Marshall, J. A. Delettrez, T. C. Sangster, R. Betti, S. C. Wilks, J. Pino, G. Kagan, K. Molvig, and A. Nikroo, Phys. Plasmas **22**, 062702 (2015).
[25]H. G. Rinderknecht, H. Sio, C. K. Li, N. Hoffman, A. B. Zylstra, M. J. Rosenberg, J. A. Frenje, M. Gatu Johnson, F. H. Séguin, R. D. Petrasso, R. Betti, V. Yu Glebov, D. D. Meyerhofer, T. C. Sangster, W. Seka, C. Stoeckl, G. Kagan, K. Molvig, C. Bellei, P. Amendt, O. Landen, J. R. Rygg, V. A. Smalyuk, S. Wilks, A. Greenwood, and A. Nikroo, Phys. Plasmas **21**, 056311 (2014).
[26]H. G. Rinderknecht, M. J. Rosenberg, C. K. Li, N. M. Hoffman, G. Kagan, A. B. Zylstra, H. Sio, J. A. Frenje, M. Gatu Johnson, F. H. Séguin, R. D. Petrasso, P. Amendt, C. Bellei, S. Wilks, J. Delettrez, V. Y. Glebov, C. Stoeckl, T. C. Sangster, D. D. Meyerhofer, and A. Nikroo, Phys. Rev. Lett. **114**, 025001 (2015).
[27]M. Gittings, R. Weaver, M. Clover, T. Betlach, N. Byrne, R. Coker, E. Dendy, R. Hueckstaedt, K. New, W. R. Oakes, D. Ranta, and R. Stefan, Comput. Sci. Discover **1**, 015005 (2008).
[28]E. L. Vold, A. S. Joglekar, M. I. Ortega, R. Moll, D. Fenn, and K. Molvig, Phys. Plasmas **22**, 112708 (2015).
[29]N. M. Hoffman, G. B. Zimmerman, K. Molvig, H. G. Rinderknecht, M. J. Rosenberg, B. J. Albright, A. N. Simakov, H. Sio, A. B. Zylstra, M. Gatu Johnson, F. H. Séguin, J. A. Frenje, C. K. Li, R. D. Petrasso, D. M. Higdon, G. Srinivasan, V. Y. Glebov, C. Stoeckl, W. Seka, and T. C. Sangster, Phys. Plasmas **22**, 052707 (2015).
[30]O. Larroche, Phys. Plasmas **19**, 122706 (2012).
[31]A. Inglebert, B. Canaud, and O. Larroche, Europhys. Lett. **107**, 65003 (2014).
[32]C. Bellei, H. Rinderknecht, A. Zylstra, M. Rosenberg, H. Sio, C. K. Li, R. Petrasso, S. C. Wilks, and P. A. Amendt, Phys. Plasmas **21**, 056310 (2014).
[33]T. Kwan, A. Le, M. Schmitt, H. Herrmann, and S. Batha, Bull. Am. Phys. Soc. **60**, 324 (2015).
[34]S. C. Hsu, T. R. Joshi, P. Hakel, E. L. Vold, M. J. Schmitt, N. M. Hoffman, R. M. Rauenzahn, G. Kagan, X.-Z. Tang, R. C. Mancini, Y. Kim, and H. W. Herrmann, EPL (Europhys. Lett.) **115**, 65001 (2016).
[35]T. R. Joshi, P. Hakel, S. C. Hsu, E. L. Vold, M. J. Schmitt, N. M. Hoffman, R. M. Rauenzahn, G. Kagan, X.-Z. Tang, R. C. Mancini, Y. Kim, and H. W. Herrmann, Phys. Plasmas **24**, 056305 (2017).
[36]C. Paquette, C. Pelletier, G. Fontaine, and G. Michaud, Astrophys. J. Suppl. Ser. **61**, 177 (1986).
[37]R. W. Schunk, Rev. Geophys. **15**, 429, https://doi.org/10.1029/RG015i004p00429 (1977).
[38]V. M. Zhdanov, *Transport Processes in Multicomponent Plasma* (Taylor & Francis, New York, 2002).
[39]J. A. Koch, T. W. Barbee, N. Izumi, R. Tommasini, R. C. Mancini, L. A. Welser, and F. J. Marshall, Rev. Sci. Instrum. **76**, 073708 (2005).
[40]H. Sio, J. A. Frenje, J. Katz, C. Stoeckl, D. Weiner, M. Bedzyk, V. Glebov, C. Sorce, M. Gatu Johnson, H. G. Rinderknecht, A. B. Zylstra, T. C. Sangster, S. P. Regan, T. Kwan, A. Le, A. N. Simakov, W. T. Taitano, L. Chacn, B. Keenan, R. Shah, G. Sutcliffe, and R. D. Petrasso, Rev. Sci. Instrum. **87**, 11D701 (2016).
[41]T. R. Boehly, D. L. Brown, R. S. Craxton, R. L. Keck, J. P. Knauer, J. H. Kelly, T. J. Kessler, S. A. Kumpan, S. J. Loucks, S. A. Letzring, F. J. Marshall, R. L. McCrory, S. F. B. Morse, W. Seka, J. M. Soures, and C. P. Verdon, Opt. Commun. **133**, 495 (1997).
[42]T. Nagayama, R. C. Mancini, D. Mayes, R. Tommasini, and R. Florido, Rev. Sci. Instrum. **86**, 113505 (2015).
[43]E. L. Vold, R. M. Rauenzahn, C. H. Aldrich, K. Molvig, A. N. Simakov, and B. M. Haines, Phys. Plasmas **24**, 042702 (2017).
[44]D. H. Sampson, H. L. Zhang, and C. J. Fontes, Phys. Rep. **477**, 111 (2009).
[45]J. Abdallah, Jr. and R. E. H. Clark, "Rate equations for plasmas in non local thermodynamic equilibrium," Los alamos Technical Report No. LA-11926, 1990.
[46]C. J. Fontes, H. L. Zhang, J. Abdallah, Jr., R. E. H. Clark, D. P. Kilcrease, J. Colgan, R. T. Cunningham, P. Hakel, N. H. Magee, and M. E. Sherrill, J. Phys. B **48**, 144014 (2015).
[47]C. J. Fontes, J. Colgan, and J. Abdallah, Jr., "Self-consistent large-scale collisional-radiative modeling," in *Modern Methods in Collisional-Radiative Modeling of Plasmas*, edited by Yu. Ralchenko (Springer, Switzerland, 2016), pp. 17–50.
[48]R. Florido, T. Nagayama, R. C. Mancini, R. Tommasini, J. A. Delettrez, S. P. Regan, V. A. Smalyuk, R. Rodrguez, and J. M. Gil, Rev. Sci. Instrum. **79**, 10E310 (2008).